

***Operando* diffuse reflectance UV-vis spectroelectrochemistry for investigating oxygen evolution electrocatalysts**

Sebastian Wahl,^[a] Sayed M. El-Refaei,^[a] Patrick Amsalem,^[b] Ana Guilherme Buzanich,^[c] Norbert Koch,^[b] and Nicola Pinna*^[a]

Affiliation

^a Institut für Chemie and IRIS Adlershof, Humboldt-Universität zu Berlin, Brook-Taylor-Straße 2, 12489 Berlin, Germany,

^b Institut für Physik and IRIS Adlershof, Humboldt-Universität zu Berlin, Brook-Taylor-Straße 6, 12489 Berlin, Germany,

^c Bundesanstalt für Materialforschung und -prüfung (BAM), Richard-Willstätter-Straße 11, 12489 Berlin, Germany

Abstract

Insights in the active structure of water splitting catalysts are crucial to evolve to a sustainable energy future based on hydrogen. Those insights can be generated by *operando* methods. We present a simple and inexpensive *operando* diffuse reflectance UV-vis spectroelectrochemical flow cell that can easily be adopted to existing spectrophotometers and other spectroscopy techniques. The applicability is demonstrated by *operando* studies on two cobalt-containing catalysts wurtzite-type $\text{Zn}_{0.35}\text{Co}_{0.65}\text{O}$ and spinel-type CoAl_2O_4 and it is supported by *ex situ* analyses tracking the changes the catalysts undergo during the oxygen evolution reaction. Clear structure-activity correlations are proposed, moreover our approach can distinguish between catalysts, where the whole material is active and those, where only the surface is active.

Introduction

For the development of earth-abundant catalysts for the oxygen evolution reaction (OER) that lay the basis for a sustainable energy future based on hydrogen from water, it is crucial to understand their active structure and the involved reaction mechanisms.¹ Therefore, adequate methods are needed to study catalysts under working conditions, i.e. *operando*. One suitable method is spectroelectrochemistry, which combines spectroscopy with electrochemical measurements.² Recent developments focused mainly on *operando* X-ray absorption spectroscopy (XAS), which is a technique able to investigate the local structure of materials or molecules.³⁻⁶ However, this technique requires extensive access to synchrotron facilities when dynamic processes or *operando* approaches need to be investigated. In addition, only a few

working groups offer this possibility. But there is more than just XAS. Spectroelectrochemistry was used first in the 1960s in combination with UV-visible absorption.⁷ In the beginning, transparent conducting glasses like indium- or fluorine-doped tin oxide (ITO, FTO) were used in transmission geometry on spectrophotometers. The technique evolved with the use of diffuse reflectance UV-vis (DRUV) spectroscopy on, e.g. gold electrodes.⁸ Various cell designs with different electrodes have been proposed since.⁹ Over the years, suppliers like Pine Research, Metrohm and BioLogic gave commercial access to transmission cells that fit in a cuvette or specialized DRUV setups that require a fibre optical probe and an appropriate spectrophotometer to measure a sample.¹⁰⁻¹² The studied samples are often applied on a screen-printed electrode (SPE).¹³⁻¹⁵

But, what if a spectrophotometer is already equipped with an integrating sphere, which collects a lot more of the scattered light, and is thus superior to fibre optics? Such a cell is to our best knowledge not commercially available. Still, some designs were proposed by researchers to be used at the reflectance port of a spectrophotometer. Widrig and Majda used a cell consisting of two glass plates, which were placed around a gold working and counter electrode, with a silver wire as quasi reference electrode. By capillary forces, the electrolyte was brought to the electrode.¹⁶ Kobielski et al. used a Quartz cuvette equipped with a platinum foil on which the catalyst was applied, in combination with a Pt auxiliary and a Ag/AgCl reference electrode that were placed behind the working electrode.¹⁷ Both methods minimize the optical path to the working electrode, but they do neither allow for bubbles to desorb from the electrode, nor do they support the cell with fresh electrolyte. To overcome these problems, we propose a spectroelectrochemical cell (SEC) design that can be easily adopted to already existing spectrophotometers equipped with DRUV equipment. To demonstrate the usability of the SEC, we performed experiments on two cobalt-containing model catalysts $\text{Zn}_{0.35}\text{Co}_{0.65}\text{O}$ and CoAl_2O_4 , both starting with Co in a tetrahedral oxygen coordination. The *ex situ* characterization of $\text{Zn}_{0.35}\text{Co}_{0.65}\text{O}$ was recently published by our group, and first structure-activity properties were proposed.¹⁸ CoAl_2O_4 has been studied elsewhere for its optical properties as well as towards the OER.^{5,19,20} Herein, we performed detailed *ex situ* characterization of the material before and after electrochemical OER by high resolution transmission electron microscopy (HRTEM), powder X-ray diffraction (pXRD), X-ray photoelectron spectroscopy (XPS), and XAS. Furthermore, we are in the position to propose clear structure-activity correlations by combining the *ex situ* findings to *operando* measurements in our presented SEC. We prove that our spectroelectrochemistry approach is able to provide insights on active phase catalysts under *operando* conditions while requiring comparatively low resources.

Results

Flow-cell design

The main design considerations for the SEC were based on minimizing the optical path to maximize the yield of reflected light. A large electrolyte reservoir was avoided by using a peristaltic pump flushing the cell with the electrolyte. By this, the evolving gases as well as dissolved species origin from the catalyst surface are carried away from the electrode. Thus, all measured activity can be assigned to the heterogeneous catalyst, and activity arising from homogeneous catalysts can be excluded. Despite of the low cell profile, a reversible hydrogen electrode (RHE) is used as the reference electrode. A schematic overview of the SEC can be found in **Fig. 1** (see Methods for detailed description and **Fig. S9** for photographs).

As a proof of concept **Fig. 2** shows two spectra taken with the same spectrophotometer configuration: $\text{Zn}_{0.35}\text{Co}_{0.65}\text{O}$ in powder form with a BaSO_4 background (a) and applied on the gold working electrode of an SPE with the bare electrode as background (b). The comparison shows an overall decreased intensity when measuring on the SPE, and a decrease in absorptions arising from Zn at lower and Co transitions at higher wavelengths. Although, the transitions of Co are clearly visible and show no energetic shift, and thus, an SPE with an Au WE is suitable to measure structural properties of cobalt containing samples.

Dry measurements of $\text{Zn}_{0.35}\text{Co}_{0.65}\text{O}$

In our previous paper, it was demonstrated how the structure of $\text{Zn}_{0.35}\text{Co}_{0.65}\text{O}$ transforms under the influence of an alkaline milieu as well as of an applied potential to promote the oxygen evolution reaction (OER).¹⁸ To get deeper understanding into the formation of the active oxygen evolution catalyst (OEC), *operando* DRUV spectroscopic measurements were performed, to connect the gained insights from *ex situ* analyses with the obtained spectra. The evolution of the spectra with applied potential can be found in **Fig. 3**.

The spectrum of the dry sample in the cell (**Fig. 3a**) shows the typical $\text{Co}^{2+}_{\text{Td}}$ (Td, tetrahedrally coordinated by four oxygen atoms) transitions at 667, 624 and 580 nm, which can be assigned to the transitions $^4\text{A}_2(\text{F}) \rightarrow ^2\text{E}(\text{G})$, $^4\text{A}_2(\text{F}) \rightarrow ^4\text{T}_1(\text{P})$ and $^4\text{A}_2(\text{F}) \rightarrow ^2\text{A}_1(\text{G})$, respectively.²¹ In comparison to the measurement on the SPE outside the cell, the overall intensity is decreased, but the transitions are at the same positions.

$\text{Zn}_{0.35}\text{Co}_{0.65}\text{O}$ in 1 M KOH

Upon wetting the sample with 1 M KOH, the electronic transitions of $\text{Co}^{2+}_{\text{Td}}$ vanish. The DRUV spectrum in 1 M KOH (**Fig. 3b** and **I** for more details) has a weak intensity compared to the spectra with an applied voltage. From the *ex situ* pXRD pattern of $\text{Zn}_{0.35}\text{Co}_{0.65}\text{O}$ in 1 M KOH, $\text{Co}(\text{OH})_2$ formation is expected, when the sample comes in contact with KOH (Fig. 1 in Reference 18). Therefore, a d^7 electron configuration in weak octahedral ligand field was assumed. A deconvolution of the absorption bands below 800 nm yielded 3 underlying bands. The first band centered at 632 nm falls in the region of the spin-allowed transition ${}^4\text{T}_{1g}(\text{F}) \rightarrow {}^4\text{A}_{2g}(\text{F})$. Since this band was reported to be of little intensity, it might be as well arising from the splitting of ${}^2\text{G}$ free ion term.²² It is followed by the likewise allowed transition ${}^4\text{T}_{1g}(\text{F}) \rightarrow {}^4\text{T}_{1g}(\text{P})$ at 533 nm. At 396 nm and below that, bands arising from the splitting of the ${}^2\text{H}$ free ion term and the mixing with other states are expected.²³ Compared to the spectra of rock salt CoO nanoparticles (**Fig. S1b**), which also contain $\text{Co}^{2+}_{\text{Oh}}$ (Oh, octahedrally coordinated by six oxygen atoms), the approximated Δ_{O} value is larger (8428 cm^{-1} vs 7711 cm^{-1} and 7326 cm^{-1}). This can be expected, as from the spectrochemical series the OH^- -ligand is a σ -donor ligand and thus induces a stronger ligand field splitting than the oxo-ligand (O^{2-}), which has more of a π -donor character.²⁴ Therefore, the *in situ* spectrum of $\text{Zn}_{0.35}\text{Co}_{0.65}\text{O}$ in 1 M KOH can be assigned to $\text{Co}^{2+}_{\text{Oh}}$. These finding confirm the previously proposed formation mechanism of the OER catalyst, which passes through a brucite-type $\text{Co}(\text{OH})_2$ intermediate.¹⁸

$\text{Zn}_{0.35}\text{Co}_{0.65}\text{O}$ at 0.9 V vs RHE

When a potential of 0.9 V is applied, only very little current is measured by chronoamperometry (CA, **Fig. 3g**). Therefore, no change in oxidation state is expected (see also the cyclic voltammograms (CV) in Reference 18). The overall intensity is increased and the relative intensities of the absorption peaks change compared to the spectrum recorded without applied potential (**Fig. 3b** and **m** for more details). The maxima of the assigned transitions are close to the previously found. While the first two transitions at 630 nm and 548 nm show no difference in relative intensity, the one at 407 nm has a much lower relative intensity. The overall increase in intensity can be understood from the observation that by inducing a positive charge on the sample, Zn^{2+} ions leach from the structure by coulomb repulsion.¹⁸ Thus, more defects are generated in the sample, which increases the mixing with transitions arising from lower symmetries than O_h , e.g. C_3 or D_{3d} (e.g. those are expected upon stretching or shrinking of an octahedron) leading to an increased absorption.^{23,25} Furthermore, the increase could be also due to spin-orbit coupling originating in the ${}^2\text{G}$ free ion terms.²²

$\text{Zn}_{0.35}\text{Co}_{0.65}\text{O}$ at 1.3 V vs RHE

The oxidation of Co^{2+} to Co^{3+} is expected between 1.0 and 1.2 V. Indeed, the corresponding CA measurements show a current increase (**Fig. 3h**), which proves the oxidation to Co^{3+} . The change in the current at 1.0 and 1.1 V points to a Faradaic current, where Co^{2+} is oxidized. The CA for the potentials 1.15 to 1.3 V shows instead mainly capacitive current, pointing to no more oxidation events. The absorption spectra reflect the electrochemical measurements, indeed the main changes take place between 1.0 V to 1.2 V indicating the oxidation of Co^{2+} to Co^{3+} . Therefore, between 1.2 and 1.3 V the predominant oxidation state is +III, so a d^6 electron configuration. **Fig. 3c** shows obvious changes in comparison to the spectrum recorded at 0.9 V. The intensity raises with increasing potential, and the maximum absorption is shifted to lower energies (1.0 V: 620 nm, 1.1 V: 640 nm, 1.15 V: 650 nm, 1.2-1.3 V: 670 nm). The vanishing of the band around 400 nm, as well as the increased absorption starting from 800 nm are also important changes. According to previous studies, the formation mechanism of an OEC from $\text{Co}(\text{OH})_2$ involves the oxidation of Co^{2+} to Co^{3+} and further to Co^{4+} .^{3,26} In a bulk material, often only the surface is affected by changes, whilst the bulk stays nearly untouched.^{4,27} Since $\text{Zn}_{0.35}\text{Co}_{0.65}\text{O}$ is a nano-sized structure with extended layers, the material could be approximately treated as a "surface-only" material. Thus, a change over the whole material is expected. Indeed, from the *ex situ* measurements after the electrochemical reaction, we demonstrated that the main phase after reaction is $\gamma\text{-Co}(\text{O})\text{OH}$.¹⁸ Also, in the literature it is consensus, that the active phase consists of $\text{Co}(\text{O})\text{OH}$ units.²⁸⁻³⁰ However, if we compare the spectrum of our *in-situ* formed $\gamma\text{-Co}(\text{O})\text{OH}$ to the spectra of other d^6 reference materials such as $\text{Co}(\text{O})\text{OH}$ and ZnCo_2O_4 (**Fig. S2**), large differences are visible. In $\text{Co}(\text{O})\text{OH}$ reference hexagonal platelets (cf. Figure SI-5 in reference 18), the first absorption covers the region between 200 and 800 nm and no absorptions are recorded between 800 nm and 1100 nm. At lower energy, a very weak $^1\text{A}_{1g}(\text{I}) \rightarrow ^3\text{T}_{1g}(\text{H})$ transition can be observed (ca. 1250 nm). The spectrum of ZnCo_2O_4 , in which only $\text{Co}^{3+}_{\text{Oh}}$ is expected, shows also an absorption minimum at around 1000 nm. In our *in-situ* formed $\gamma\text{-Co}(\text{O})\text{OH}$ sample, however, the onset of the first band lies at around 500 nm and strong absorptions are also observed between 800 and 1400 nm in the NIR region (**Fig. 3c** and **S3a**).

When applying the Tanabe-Sugano theory for octahedral symmetry with a d^6 electron configuration in a strong ligand field, within reasonable values for B and Δ_{O} no bands are expected above 850 nm as the spectra of the reference materials show (**Fig. S2**). On the other hand, the spectrum of $\text{Zn}_{0.35}\text{Co}_{0.65}\text{O}$ at 1.3 V shows a broad absorption between 500 and 1400 nm and thus it is reasonable to assume a lower symmetry than O_h . This assumption is also based on the *ex situ* EXAFS measurements that showed a cobalt coordination number of 5.6.¹⁸ Since one metal center can only hold a natural number of ligands, a linear combination of

sixfold and five- or less-coordinated Co could give a good approximation. Extreme cases of five-coordinated Co would be a square pyramid with C_{4v} geometry or a trigonal bipyramidal structure with D_{3h} geometry.³¹⁻³³ The continuous absorption above 700 nm could be attributed to electrochromism. Electrochromism is ascribed to the oxidation of the central ion and subsequent intercalation of OH^- ions into the material to maintain electroneutrality under an anodic potential.³⁴⁻³⁶ Thus, cobalt containing materials, namely Co_3O_4 , are colored, i.e. increased absorption, upon anodic potential and bleached under cathodic potential.³⁷⁻⁴⁰ Therefore, electrochromism causes a change of the band structure and of the geometry around the central ion. The Fermi-level is lowered, and thus electrons can get easier excited to the conduction band.

Zn_{0.35}Co_{0.65}O at 1.4 V vs RHE

The CA shows Faradaic current when the potential is increased to 1.4V (**Fig. 3i**), which can be attributed to the oxidation of Co^{3+} to Co^{4+} , as also depicted by the shoulder in the CV (Fig. 5a in Ref. 18). The intensity of the absorption spectrum in **Fig. 3d** increases and the absorption maximum shifts to lower energies (690 nm). As the active OEC is based on changes in oxidation state between +III and +IV, also the DRUV spectrum is expected to contain at least two species. The observed increase of absorption at higher wavelengths is in accordance to measurements done by Webster et al. for molecular Co^{4+}_{Oh} species.⁴¹ Contrary to those findings, the missing absorption at lower wavelengths points to a deviation from O_h symmetry.

Zn_{0.35}Co_{0.65}O at OER potential

From an applied potential of 1.45 V, the current shows no more decreasing when the potential is raised. Indeed, the observed stationary current can be attributed to the evolution of O_2 . At 1.55 V, a current density of 10 mAcm^{-2} is reached. The CA in **Fig. 3k** shows oscillations, which can be ascribed to the evolution of bubbles on the electrode and the inhibited mass transport of electrolyte to the electrode surface. The results are also clearly visible in the spectra in **Fig. 3e**. Especially in the lower energy regime, the noise increases more for the previous measurements. The absorption maximum is further shifted to lower energies (1.45 V: 700 nm, 1.6 V: 720 nm), and the intensity is slightly increased. The general shape of the absorption band is not changed, and thus also major changes in structure are not expected between 1.3 V and OER potential. To validate the measurements, the *operando* spectra were also measured for the $Co(O)OH$ reference hexagonal platelets (**Fig. S4**). The spectra show the same electrochromism and also the same trend in the shift of absorption maxima. This further proves that the $Co(O)OH$ reference phase shows a similar behavior as our *in-situ* formed γ - $Co(O)OH$,

that is, due to its layered structure most of the material is involved in the water oxidation process.

Zn_{0.35}Co_{0.65}O reduction

When reducing the potential to 1.1 V, the reversed effect as for the oxidation can be observed in **Fig. 3n-p**. The CAs from 1.4 to 1.1 V show a small negative current, which indicates the reduction of the Co⁴⁺ species. In the spectra, the intensity decreases with every potential decrease and the absorption maximum is shifted to higher energies (1.1 V: 630 nm). **Figure S3b** shows almost overlapping between the spectra recorded at 1.3 V under anodic and cathodic potential. There is only minor differences in the intensity, and the maximum absorption is at the same value (673 nm). This proves that the geometrical and electronic structure changes under OER conditions are reversible.

Characterization of CoAl₂O₄

After measuring the optical response of a structure that is known to change its phase during the reaction, another structure was studied. CoAl₂O₄ in the spinel structure was synthesized by the “benzyl alcohol route”. This was achieved by using cobalt(II) acetate and aluminum triisopropoxide as metal precursors and benzyl alcohol as oxygen source, solvent and surface stabilizing agent.^{20,42,43} After 48 h at 250 °C in a PTFE-lined steel autoclave, the sample was washed with ethanol, solid products were collected by centrifugation and the sample was dried overnight at 70 °C. A blue powdered product was obtained.

The crystal structure of CoAl₂O₄ was identified by pXRD. Only typical reflections of the cubic spinel structure (ICSD PDF-number 01-070-0753)⁴⁴ were present in the pattern in **Fig. 4a**. Using the Scherrer equation, a mean crystallite size of 5.6 nm was calculated.

Insight in the oxidation state of CoAl₂O₄ was gained by characterizing the chemical surface of the sample by XPS (**Fig. 4b**). The Co2p_{3/2} peak is at 781.8 eV, with a shake-up satellite shifted by 5.5 eV. The Co2p_{1/2} peak is shifted by 15.6 eV compared to Co2p_{3/2}. Compared to previous works, this indicates an oxidation state of +II for cobalt.^{18,45,46} The Al2p_{3/2} peak (**Fig. S5a**) is at 74.1 eV, which points to Al³⁺ in an oxygen environment.¹⁹ In the spectrum on the Al edge, some signal from gold is visible. This is likely due to bare gold electrode patches, on which the spectra were measured (see supporting information for more details).

HRTEM analyses of CoAl₂O₄ before the reaction in **Fig. 5 a-c** show particles with a high crystallinity and with a mean size of 6.0 ± 1.4 nm, which is in good accordance to the crystallite

size estimated by pXRD. The selected area electron diffractogram (SAED) shows the expected reflections of the CoAl_2O_4 phase with 311 as the most intense reflection (**Fig. 5b**).

Energy dispersive X-ray spectroscopic (EDX) analyses (see **Table 1**) yield a cobalt to aluminum ratio of 35.2 % to 64.8 % for CoAl_2O_4 , confirming the expected stoichiometry of both metals in the material. The EDX mapping in **Fig. S7** shows the uniform distribution of the metals in the material.

The DRUV spectrum in **Fig. S1a** shows the typical absorptions for $\text{Co}^{2+}_{\text{Td}}$ at 634, 577 and 549 nm, which can be assigned to the transitions $^4\text{A}_2(\text{F}) \rightarrow ^2\text{E}(\text{G})$, $^4\text{A}_2(\text{F}) \rightarrow ^4\text{T}_1(\text{P})$ and $^4\text{A}_2(\text{F}) \rightarrow ^2\text{A}_1(\text{G})$, respectively.²¹ The fine splitting of the transition $^4\text{A}_2(\text{F}) \rightarrow ^4\text{T}_1(\text{F})$ is visible between 1800 to 1000 nm. At 1362 nm, the $2\nu(\text{OH})$ harmonic band from residual surface OH-groups is observed.⁴⁷ Below 500 nm, a very strong absorption is visible, which could involve charge-transfer processes as well as transitions the free-ion ^2H term, which is split in the tetrahedral field. It might be also arise from octahedrally coordinated cobalt due to inversion of sites in the spinel structure.^{48,49}

Electrocatalytic activity toward the OER was examined by rotating disk electrode (RDE) measurements in 1 M KOH. The CVs of CoAl_2O_4 at different scan rates are shown in **Fig. 6a**. The small anodic and cathodic peaks at ~ 1.06 V can be assigned to the redox-couple $\text{Co}^{2+}/\text{Co}^{3+}$. At ~ 1.43 V, peaks indicate the redox-pair $\text{Co}^{3+}/\text{Co}^{4+}$. The presence of anodic and cathodic peaks indicates a reversible reaction. At around 1.53 V, the onset of the OER starts.

From the power law relationship between the oxidation peak current (i) and the scan rate (v), $i = av^b$, it can be estimated, whether a surface or bulk redox process is taking place. a and b are adjustable parameters, and b can be expressed as the slope of the plot of $\log(i)$ vs $\log(v)$. When b is close to 0.5, a Faradaic redox process in the bulk is indicated, while b being close to 1.0 indicates a surface-limited redox process.^{50,51} When fitting the slope of $\log(i)$ vs $\log(v)$ (**Fig. 6a inset**), we obtain 0.9 as the b value for the redox-couple $\text{Co}^{2+/3+}$, indicating a surface-limited reaction for CoAl_2O_4 .

The linear sweep voltammograms (LSV) in **Fig. 6b** shows the activity of CoAl_2O_4 compared to $\text{Zn}_{0.35}\text{Co}_{0.65}\text{O}$ and $\text{Co}(\text{O})\text{OH}$. The average overpotential towards the OER lies at 362 mV ($\text{Zn}_{0.35}\text{Co}_{0.65}\text{O}$: 322 mV, $\text{Co}(\text{O})\text{OH}$: 382 mV) at a current density of 10 mAcm^{-2} . The electrochemically active surface area (ECSA) was determined from the double-layer capacitance according to McCrory et al. (**Fig. S6**).⁵² It lies at 1.13 cm^2 , and is thus smaller than the one of $\text{Zn}_{0.35}\text{Co}_{0.65}\text{O}$ (21.93 cm^2) and $\text{Co}(\text{O})\text{OH}$ (5.71 cm^2). The electrochemical performance is comparable to spinel type Co_3O_4 .¹⁸

To analyze the influence of the OER on the material, it was held for 1 h at a current density of 10 mAcm^{-2} . In the XPS spectrum after the reaction in **Fig. 4b**, the $\text{Co}2p_{3/2}$ peak position is at 781.3 eV, and the shake-up satellite is shifted by ca. 5.5 eV. The $\text{Co}2p_{1/2}$ peak is shifted by 15.6 eV compared to $\text{Co}2p_{3/2}$. For Co^{3+} species the shake-up satellite is expected to be shifted by 10.0 eV compared to the $\text{Co}2p_{3/2}$.⁴⁵ Here, the markedly unchanged line shape of the $\text{Co}2p$ spectrum after reaction points towards the same oxidation state as before reaction. The $\text{Al}2p_{3/2}$ peak (**Fig. S5a**) is shifted to 73.6 eV and can be assigned to Al^{3+} in an oxygen environment. The 0.5 eV energy shift of the Co and Al main peak positions can be attributed to small changes in the Fermi level of the thin films. This is further supported by the fact, that the oxygen main peak is shifted by the same amount (see **Fig. S5c**). From XPS it should be concluded that no major changes in oxidation state occur upon reaction.

The HRTEM micrographs after reaction in **Fig. 5 d-e** show close aggregated particles. The SAED pattern in **Fig. 5e** shows one phase, that can be assigned to spinel-type CoAl_2O_4 . Also the power spectral analysis indicates no second crystalline phase. On the other hand, as the reflections of pure Co_3O_4 are expected at nearly the same position as for CoAl_2O_4 , no distinction between those can be made.

The EDX analysis after the reaction (see **Table 1**) yields a cobalt to aluminum ratio of 40 % to 60 %, indicating a little loss of aluminum from the material.⁵³ The EDX mapping in **Fig. S8**, however, shows a uniform distribution of Co and Al in the particles. Following Lippens and Lannoo, for particles of $6.0 \pm 1.4 \text{ nm}$ size, 11 – 18 % of all atoms are located on the surface of a particle. Thus, the amount of Al leached can be attributed to the top most layer (see SI for details).⁵⁴

Analysis of the X-ray absorption near-edge structure (XANES) spectra (**Fig. 4c**) shows no change in the edge energy (7718.0 eV) between CoAl_2O_4 before and after 1 h electrochemical reaction at 10 mAcm^{-2} . Also, in the fingerprint region after the edge, only little difference is visible. This is in accordance to the XPS results indicating no change in the oxidation state after the reaction.

Extended X-ray absorption fine structure (EXAFS) (**Fig. 4d**) of the sample before and after the reaction also shows high similarity. Unfortunately, the EXAFS before the reaction could not be fitted with just a simple model based on the crystal structure of CoAl_2O_4 , probably due to the partial inversion of Co and Al sites in the spinel structure and also the high surface to volume ratio in the small nanoparticles.^{48,49} A fit of the EXAFS after the reaction, however, was possible in the range from 1.15 to 3.6 \AA , assuming a spinel unit cell without defects. The peak at a

reduced distance of 2.00 Å corresponds to 4 oxygen atoms tetrahedrally coordinated around the central cobalt atom. The second shell is composed of 12 aluminum atoms in a reduced distance of 3.29 Å, 12 oxygen atoms at 3.33 Å and 4 cobalt atoms at 3.44 Å. The other fitting parameters can be found in **Table S9**. From comparison to the fit after reaction and with Maurizio et al.,⁴⁹ a qualitative analysis of the spectrum before the reaction can be done. The first peak must be from the oxygen coordinated around the cobalt atom. The second peak is less pronounced and a bit broader than after reaction, indicating less regular features that dissolve during the reaction. The third peak is at around the same position as after the reaction, but shows no shoulder. All in all, the EXAFS analysis of the samples also show no significant change in the main features after the reaction.

To conclude, the *ex situ* characterization of CoAl₂O₄ before and after the reaction indicate no significant change in the main crystalline structure. The loss of Al detected by EDX can be ascribed to the top-most surface layer of the nanoparticles, but an additional change in the surface structure could not be detected by our experiments.

Operando measurement of CoAl₂O₄

CoAl₂O₄ nanoparticles were also measured by *operando* DRUV spectroscopy. In contrast to Zn_{0.35}Co_{0.65}O, where the sample undergoes a phase transformation, here no significant changes in the structure could be observed after the OER. The spectra recorded under anodic potential in **Fig. 7a** show no shift in the peak positions compared to the spectrum of powdered CoAl₂O₄ nanoparticles (**Fig. S1a**), nor are there new bands visible. Only the intensity is slightly increased upon increasing potential, and might be again attributed to electrochromism. The increase of the bands below 500 nm and above 800 nm at 1.6 and 1.65 V are most probably due to the evolution of O₂ bubbles (cf. **Fig. 7 c** and **f**, indeed for applied potentials above 1.55 V the recorded current is above 10 mA/cm²). Also for the spectra recorded under cathodic potential (**Fig. 7d**), only a slight decrease in the intensity can be observed. These spectra prove that the “bulk” of the material (even though the particle size is below 10 nm) is unaffected even under anodic potential, where the oxidation of cobalt to +IV species is expected. This is in line with the CV analysis, which points to redox reactions confined at the top most surface of the nanoparticles.⁵¹ Additional structural characterizations before and after electrochemistry support our conclusions. As a matter of fact, SAEDs are unchanged (cf. **Fig. 5 b** and **e**) and no additional phases could be detected. Moreover, STEM EDX mapping shows no change in the Al and Co distribution over the nanoparticles. On the other hand, a slight decrease of the Al concentration is recorded (few atom%, **Table 1**), pointing to the partial leaching of Al at the top most surface of the nanoparticles leading to reorganization of the surface. All in all, the

operando DRUV studies match the *ex situ* structural and chemical characterizations and demonstrate that only the first atomic layers of the CoAl_2O_4 nanoparticles are active towards the OER.

Discussion

The use of *operando* DRUV spectroscopy, together with our newly developed electrochemical flow cell, appears to be well suitable for the study of changes in the local structure of electrocatalysts under working conditions. Indeed, the *operando* measurements permitted to accurately follow the structural changes the $\text{Zn}_{0.35}\text{Co}_{0.65}\text{O}$ precatalyst undergoes, i.e. when it gets in contact with KOH and when a potential is applied. The observations in low potential regions could be analyzed and the results could be correlated to *ex situ* measurements. Thus, deeper insights in the formation mechanism of the active cobalt species could be gained. From a pure tetrahedral coordination of Co^{2+} the whole Wurtzite-type $\text{Zn}_{0.35}\text{Co}_{0.65}\text{O}$ material underwent a structural change to an octahedral Co^{2+} coordination (i.e. $\text{Co}(\text{OH})_2$), without changing its oxidation state. When an anodic potential is applied, the oxidation state changes to +III (above 1.1 V) and +IV (above 1.4 V). The oxidation is coupled to a decrease of the symmetry around the central ion (transition from O_h to either square pyramid C_{4v} or trigonal bipyramid D_{3h}), which could not be analyzed by other available experimental tools. Furthermore, it could be shown that at the OER potential (i.e. > 1.5 V) a significant amount of Co^{3+} is still present as only little shift of the absorption maximum could be observed compared to lower anodic potential (e.g. 1.3 V). This is in good agreement with the literature and the proposed mechanism for the OER, where the active centers switch the oxidation state between +III and +IV and involve either oxygen vacancies or peroxide species.^{3,55-57} It was also shown, that the formation of the active phase is a reversible process, as the spectra after the cathodic potential did not differ essentially from the ones under anodic potential. Nevertheless, it was shown that electrochromism cannot be neglected when measuring DRUV spectra at elevated potentials. The spectra recorded at 1 V and above show limitations of the *operando* DRUV technique. Since UV-Vis absorption spectroscopy probes the valence electrons, it is very sensitive to small changes in the electronic structure of a sample. On the other hand, the assignment of certain bands is in some cases very difficult, as the electronic terms can split further into fine structures depending on the ligand field geometry. Also, the electrochemically induced redox reactions lead to a variation of the ground state, further complicating the analysis. Finally, the OER has also an influence on the UV-Vis spectra. Indeed, it induces the formation and breaking of bonds, and dynamical changes on the electron configuration and on the local structure around the probed metal center.

Moreover, only few electrocatalytical materials involve the whole bulk-structure as the active phase. For most materials, only the surface shows catalytic activity. As an example for this, CoAl_2O_4 was used as a model catalyst. The electrochemical data showed a high activity towards the OER, but in the *operando* DRUV measurements, in accordance to the *ex situ* characterization, no structural changes were visible. In particular, the clear signature of the Co^{2+} ions in tetrahedral environment is unaffected. Thus, it is valid to assume that the catalytically active centers are on the top first atomic layers only. The inertia of the underlying tetrahedrally coordinated cobalt further indicates that the assignment of the active phase to one certain structure is not straightforward.

Interestingly, although the ECSA of CoAl_2O_4 is among the smallest of the studied systems, it has a significant activity towards the OER. This means it has a higher activity per center compared to the other materials studied, indicating that on these centers the structures for the OER are optimized. On the downside, fewer centers are available. Thus, new syntheses should strive to even smaller particles, to increase the number of active centers. Nevertheless, we showed that by combining DRUV measurements and *ex-situ* chemical and structural analyses valuable information can be acquired even on materials bearing only surface catalytic species.

One of the advantages of the presented spectroelectrochemical technique lies in its wide accessibility when combined with the simple and inexpensive flow cell we have developed. By modifying the mount of our cell, it can be fitted to any DRUV spectrophotometer with very little effort. By using a Quartz window, also the NIR range is accessible. Moreover, the cell can be easily adapted to other experiments, for example by replacing the Quartz window with a Kapton™ foil the setup can be applied to *operando* XAS measurements in fluorescence mode and in XRD in Bragg-Brentano geometry.

All in all, our approach tries to bridge the gap between model catalysts studied by surface science techniques under UHV and catalyst materials studied under highly concentrated electrolytes and we are convinced that the electrocatalysis community will adopt it as a standard *operando* tool.

Methods

Chemicals: All reagents were used as received. Cobalt(II) acetate (anhydrous, 98 %) was purchased from ABCR GmbH (Karlsruhe, Germany). Aluminum triisopropoxide (anhydrous, 98 %) and benzyl alcohol (puriss.) were purchased from Sigma Aldrich (Munich, Germany). Absolute ethanol (EMPARTA) was purchased from VWR International GmbH (Darmstadt, Germany). 1 N potassium hydroxide solution was purchased from Carl Roth GmbH (Karlsruhe, Germany).

Materials for the SEC: MetalVelvet™ black foil sheet, low outgassing adhesive (ACM Coatings GmbH, Naumburg, Germany). PEEK raw part (Grünberg Kunststoffe, Berlin, Germany). PTFE raw part (ADS Drehservice GmbH, Ahaus, Germany). Quartz glass cover slip, Ø18 mm, 0.25 mm thick (Plano GmbH, Wetzlar, Germany). Silicone sheet, white, 0.5 mm thick, ~60 Sh-A (Modulor GmbH, Berlin, Germany). To seal small leakings: One components silicone rubber Scrintec® 600, oxime cross-linking (Carl Roth GmbH, Karlsruhe, Germany). 0.8 mm diameter PTFE tubing, flanged (VWR International GmbH, Darmstadt, Germany).

Syntheses: Syntheses of $\text{Zn}_{0.35}\text{Co}_{0.65}\text{O}$, ZnCo_2O_4 , $\text{Co}(\text{O})\text{OH}$ and CoO were described before.¹⁸ CoAl_2O_4 was synthesized by adding cobalt(II) acetate (248 mg, 1.4 mmol, 1 eq.) and aluminium triisopropoxide (572 mg, 2 mmol, 2 eq.) to benzyl alcohol (25 mL) in a 45 mL PTFE-lined stainless steel autoclave (Parr Instruments GmbH, Frankfurt, Germany) equipped with a stirring bar in an argon atmosphere. After sealing the autoclave, it was placed on a stirring plate and stirred for 2 h to dissolve all solids. Then, it was heated at 250 °C for 48 h. After cooling, product was obtained as a blue dispersion. Collecting the solid product by centrifugation and washing with ethanol was challenging, as the dispersion formed in benzyl alcohol as well as in ethanol was very stable. After washing, the product was dried at 70 °C in an oven. 185 mg of a blue product were obtained (74 % yield based on precursor's stoichiometry).

Flow cell design: The front part is made from polyether ether ketone (PEEK), which is covered with a black foil (MetalVelvet™, ACM Coatings GmbH) with a 4 mm hole, to only reflect light from the working electrode. The front is placed on a mount and hold by magnets at the reflectance port of the spectrophotometer. In the main area, the PEEK has a thickness of 2 mm. A 0.25 mm thick Quartz window is embedded in the PEEK and allows the light to pass to the working electrode and back. It also allows for measurements in the near-infrared (NIR) range. An SPE (DropSens 250AT, Metrohm) is used as the substrate for the catalyst and is connected via a 2 pin connector cable (2.54 mm contact spacing) to the potentiostat. The catalyst is placed on the 4 mm Au electrode, and the Pt ring around acts as the counter electrode. The SPE is placed in silicone gaskets that direct the flow of the electrolyte. The front gasket is 0.5 mm thick and thus

the volume in front of the electrode is $\sim 50 \mu\text{L}$. The total distance from the electrode to the reflectance port is only $\sim 2.5 \text{ mm}$. The electrolyte passes through the channel in front of the electrode and the 2 mm diameter channels in the back part of the SEC, which is made from polytetrafluoroethylene (PTFE). It is connected by PTFE tubes with HPLC fittings to the peristaltic pump and the waste bottle. The electrolyte is pumped at a rate of 0.92 mL/min through the system and thus the solution in front of the electrode is renewed ~ 18 times per minute. The tip of the RHE reference electrode (Mini HydroFlex[®], gaskatel) is in contact to the electrolyte in the inlet channel to allow for a controlled potential in the cell. Wing bolts and nuts tighten the setup. A 3D-printed cover with holes for the tubes, cables and RHE protects the cell from ambient light. Additionally, the system is covered with a black tissue. Blueprints are available upon request from the corresponding author.

Characterization: XRD diffraction patterns were obtained using a STOE STADI MP (STOE, Darmstadt, Germany) running at $U = 50 \text{ kV}$ and $I = 40 \text{ mA}$ with $\text{Mo K}\alpha = 0.70930 \text{ \AA}$ monochromatic radiation (using a Ge(111) monochromator) and a DECTRIS "MYTHEN 1K" detector. The patterns were recorded in 2θ geometry in the range of 4 to 60° .

HRTEM images and EDX mappings were obtained using a FEI Talos F200S operated at 200 kV scanning/transmission electron microscope (S/TEM). Particle sizes were estimated by measuring 250 particles manually.

X-ray photoelectron spectroscopy (XPS) was performed in an ultrahigh vacuum chamber (base pressure $5.10\text{-}10 \text{ mbar}$) using a JEOL JPS-9030 set-up comprising a hemispherical photoelectron spectrometer and a monochromatic $\text{Al K}\alpha$ ($h\nu = 1486.6 \text{ eV}$) X-ray source. The XPS measurements were performed with an energy resolution of 1.25 eV as determined on a polycrystalline $\text{Ag } 3d$ core level. The samples were directly measured on SPEs. The spectra were corrected for charging by shifting the $\text{C } 1s$ peaks to 284.8 eV .

XANES and EXAFS measurements of the samples before electrochemical reaction were performed at the BAMline (BESSY-II, Helmholtz Centre Berlin for Materials and Energy Berlin, Germany). The beam was monochromatized using a double-crystal monochromator (DCM). The size of the beam was $3 \times 1 \text{ mm}$. The measurements were performed at Co-K edge (7709 eV) in transmission geometry, with two ionization chambers as detectors. The excitation energy was varied from 7614 eV to 8428 eV , with varying energy steps. For the pre-edge region, the energy was varied in 10 eV steps; for the region around the edge, energy was tuned in 0.5 eV steps and in the EXAFS region with a constant step in the k -space of 0.04 \AA^{-1} . The associated uncertainty was experimentally determined by measuring the cobalt metal foil 10

times. A value of ± 0.3 eV was obtained. For the measurement, the samples were mixed with boron nitride and fixed in plastic sample holders. Before collecting the sample spectra, a cobalt foil was used as a reference for the cobalt edge. The relative energies of the spectra were calibrated to the first inflection point of the cobalt metal absorption edge. To determine the edge energy, the first inflection point was used. EXAFS data were processed by ATHENA and ARTEMIS from Demeter version 0.9.26.⁵⁸ This GUIs program belongs to the main package IFEFFIT (v. 1.2.12).⁵⁹

Electrochemical analyses were performed using a Bio-Logic VMP3 multichannel potentiostat/galvanostat with a built-in EIS analyzer. The electrochemical behavior and activity of catalysts were measured in a three-electrode electrochemical cell using a 3 mm diameter glassy carbon rotating disc electrode (RDE, Autolab RRDE, Metrohm, Filderstadt, Germany) operated at 1600 rpm at 25 °C. A platinum wire was used as the counter electrode and a reversible hydrogen electrode (HydroFlex, gaskatel, Kassel, Germany) was used as a reference electrode. The electrodes were prepared by drop casting 3 μ L of a catalyst ink onto glassy carbon. The ink was prepared by sonicating 1 mg catalyst powder with 490 μ L ethanol, 490 μ L purified water and 20 μ L Nafion for 30 min.

The sample after reaction for the HRTEM and XAS analyses was prepared by dropcasting an ethanolic dispersion of the CoAl_2O_4 onto a nickel foil, performing 1 h chronopotentiometry at a current density of 10 mA cm^{-2} , rinsing the foil with ethanol and scratching off the material. This was repeated several times.

DRUV spectroscopy was performed on a PerkinElmer LAMBDA 950 UV/Vis Spectrophotometer equipped with a 150 mm integrating sphere. Powdered samples were measured at the reflectance sample holder port, by mixing them with a small amount of BaSO_4 . Spectra were measured in the wavelength range between 2500 and 200 nm. For baseline detection, pure BaSO_4 was used, and the Kubelka-Munk function was used to compute the spectra.

Operando DRUV measurements were performed in the cell described above and in the predecessor model (supporting information and **Figure S10**). A 4 mm gold screen-printed electrode (DropSens 250AT, Metrohm, Filderstadt, Germany). Screen-printed platinum was used as the counter electrode and a reversible hydrogen electrode (Mini HydroFlex[®], gaskatel, Kassel, Germany) was used as the reference electrode. The cell was connected to a BioLogic SP50 portable single channel potentiostat / galvanostat. The cell was placed at the reflectance sample holder port of the above mentioned spectrophotometer, and covered with a 3D-printed cover and a black tissue. For baseline detection, a blank SPE was used. The samples were prepared by drop casting 2 μ L of a catalyst ink on the Au electrode of the SPE. The catalyst ink

was prepared by dispersing 5 mg of catalyst powder in 1 mL ethanol using an ultrasonic bath. The spectra were collected in the range between 1000 and 350 nm with a resolution of 1 nm. 1 M KOH was used as the electrolyte, and the flow was controlled to 0.92 mL/min by a tubing pump (flow rate 0.03 to 8.20 mL/min, neoLab Migge GmbH, Heidelberg, Germany). The spectra were measured 30 s after a new potential was applied, respectively. All spectra were exported as csv-files by the spectrometers software and treated further with OriginPro 2017. Spectra then were computed using the Kubelka-Munk function. The band positions were obtained manually by selecting the maximum intensity of a band or the position of a shoulder or by Gaussian peak deconvolution. The band positions then were compared to the corresponding online available Tanabe-Sugano diagram via a self-written Python 3 script, and the most probable transitions were assigned.⁶⁰ The most probable band assignment based on this method can be found in the supporting information for the spectra shown (**Table S1-S8**).

Acknowledgements

Special thanks to Bernd Lück, Sven Zillmann and Bettina Röder (workshops of HU Berlin and BAM) for design considerations and manufacturing the SEC. Thanks to Christoph Erdmann for measuring HRTEM and S/TEM. S.M.E. is grateful for Yousef Jameel Scholarship Fund. Special thanks to Fabian Müller for the fruitful discussions about electronic transitions.

Author contributions

S.W. and N.P. have designed the study, analyzed the data and wrote the paper. P.A. provided XPS measurements and analysis. S.M.E. provided electrochemical measurements. A.G.B. provided XAS measurements and guidance to the interpretation. N.K. contributed to the interpretation of the XPS results.

Competing interests: The authors declare no competing interests.

Keywords: operando • spectroelectrochemistry • DRUV • cobalt • structure-property relationships

References:

- 1 United Nations. Transforming our world: The 2030 agenda for sustainable development. *Resolution adopted by the General Assembly*, (2015).
- 2 Gale, R. J. *Spectroelectrochemistry: theory and practice*. (Plenum Press, New York and London, 1988).
- 3 Bergmann, A. *et al.* Unified structural motifs of the catalytically active state of Co (oxyhydr) oxides during the electrochemical oxygen evolution reaction. *Nat. Catal.* **1**, 711, (2018).
- 4 Menezes, P. W. *et al.* Uncovering the prominent role of metal ions in octahedral versus tetrahedral sites of cobalt–zinc oxide catalysts for efficient oxidation of water. *J. Mater. Chem. A* **4**, 10014-10022, (2016).
- 5 Wang, H.-Y. *et al.* In operando identification of geometrical-site-dependent water oxidation activity of spinel Co₃O₄. *J. Am. Chem. Soc.* **138**, 36-39, (2015).
- 6 Friebe, D. *et al.* Identification of Highly Active Fe Sites in (Ni,Fe)OOH for Electrocatalytic Water Splitting. *J. Am. Chem. Soc.* **137**, 1305-1313, (2015).
- 7 Kuwana, T., Darlington, R. K. & Leedy, D. W. Electrochemical Studies Using Conducting Glass Indicator Electrodes. *Anal. Chem.* **36**, 2023-2025, (1964).
- 8 Takamura, T., Takamura, K., Nippe, W. & Yeager, E. Specular Reflection Studies of Gold Electrodes in situ. *J. Electrochem. Soc.* **117**, 626-630, (1970).
- 9 León, L. & Mozo, J. D. Designing spectroelectrochemical cells: A review. *TrAC, Trends Anal. Chem.* **102**, 147-169, (2018).
- 10 Pine Research Instrumentation. *Honeycomb Spectroelectrochemical Cell Kit*, <<https://pineresearch.com/shop/products/spectroelectrochemistry/honeycomb-cell-kit/honeycomb-spectroelectrochemical-cell-2/>> (2019).
- 11 Metrohm. *DropSens product website*, <http://www.dropsens.com/en/screen_printed_electrodes_pag.html> (2019).
- 12 Bio-Logic Science Instruments. *SpectroElectrochemistry*, <[https://www.bio-logic.net/accessories/spectroelectrochemistry/?filter\[division\]=ec-lab](https://www.bio-logic.net/accessories/spectroelectrochemistry/?filter[division]=ec-lab)> (2019).
- 13 González-Diéguez, N., Colina, A., López-Palacios, J. & Heras, A. Spectroelectrochemistry at Screen-Printed Electrodes: Determination of Dopamine. *Anal. Chem.* **84**, 9146-9153, (2012).
- 14 Thiagarajan, N., Chang, J.-L., Senthikumar, K. & Zen, J.-M. Disposable electrochemical sensors: A mini review. *Electrochem. Commun.* **38**, 86-90, (2014).
- 15 Li, M., Li, Y.-T., Li, D.-W. & Long, Y.-T. Recent developments and applications of screen-printed electrodes in environmental assays—A review. *Anal. Chim. Acta* **734**, 31-44, (2012).
- 16 Widrig, C. A. & Majda, M. Mediated, thin-layer cell, coulometric determination of monomolecular films of trichlorosilane viologen derivatives at gold and nonconducting surfaces. *Anal. Chem.* **59**, 754-760, (1987).
- 17 Kobielski, M., Pilarczyk, K., Świętek, E., Szaciłowski, K. & Macyk, W. Spectroelectrochemical analysis of TiO₂ electronic states – Implications for the photocatalytic activity of anatase and rutile. *Catal. Today* **309**, 35-42, (2018).
- 18 Wahl, S. *et al.* Zn_{0.35}Co_{0.65}O – A Stable and Highly Active Oxygen Evolution Catalyst Formed by Zinc Leaching and Tetrahedral Coordinated Cobalt in Wurtzite Structure. *Adv. Energy Mater.* **9**, 1900328, (2019).
- 19 Duan, X., Pan, M., Yu, F. & Yuan, D. Synthesis, structure and optical properties of CoAl₂O₄ spinel nanocrystals. *J. Alloys Compd.* **509**, 1079-1083, (2011).
- 20 Karmaoui, M. *et al.* Synthesis of cobalt aluminate nanopigments by a non-aqueous sol–gel route. *Nanoscale* **5**, 4277-4283, (2013).
- 21 Weakliem, H. A. Optical spectra of Ni²⁺, Co²⁺, and Cu²⁺ in tetrahedral sites in crystals. *J. Chem. Phys.* **36**, 2117-2140, (1962).

- 22 Lever, A. B. *Inorganic electronic spectroscopy* / A.B.P. Lever. 2nd ed. edn, (Amsterdam [u.a.] : Elsevier, 1986).
- 23 Andrut, M. & Wildner, M. Superposition model analysis from polarized electronic absorption spectra of Co^{2+} in trigonally distorted octahedra in brucite-type $\text{Co}(\text{OH})_2$. *Journal of Physics: Condensed Matter* **13**, 7353-7353, (2001).
- 24 Figgis, B. N. & Hitchman, M. A. *Ligand Field Theory and Its Applications*. (Wiley-VCH, 2000).
- 25 Rückamp, R. *et al.* Optical study of orbital excitations in transition-metal oxides. *New Journal of Physics* **7**, 144-144, (2005).
- 26 Gerken, J. B. *et al.* Electrochemical Water Oxidation with Cobalt-Based Electrocatalysts from pH 0–14: The Thermodynamic Basis for Catalyst Structure, Stability, and Activity. *J. Am. Chem. Soc.* **133**, 14431-14442, (2011).
- 27 Risch, M. *et al.* Water oxidation by amorphous cobalt-based oxides: in situ tracking of redox transitions and mode of catalysis. *Energy Environ. Sci.* **8**, 661-674, (2015).
- 28 Smith, R. D. L., Prévot, M. S., Fagan, R. D., Trudel, S. & Berlinguette, C. P. Water Oxidation Catalysis: Electrocatalytic Response to Metal Stoichiometry in Amorphous Metal Oxide Films Containing Iron, Cobalt, and Nickel. *J. Am. Chem. Soc.* **135**, 11580-11586, (2013).
- 29 Koza, J. A., Hull, C. M., Liu, Y.-C. & Switzer, J. A. Deposition of $\beta\text{-Co}(\text{OH})_2$ Films by Electrochemical Reduction of Tris(ethylenediamine)cobalt(III) in Alkaline Solution. *Chem. Mater.* **25**, 1922-1926, (2013).
- 30 Burke, M. S., Kast, M. G., Trotochaud, L., Smith, A. M. & Boettcher, S. W. Cobalt–iron (oxy) hydroxide oxygen evolution electrocatalysts: the role of structure and composition on activity, stability, and mechanism. *J. Am. Chem. Soc.* **137**, 3638-3648, (2015).
- 31 Wood, J. S. & Greene, P. T. Ligand field theory for pentacoordinate molecules. II. Crystal field-spin-orbit coupling treatment of the d_1 , d_3 , d_6 , and d_8 configurations in trigonal-bipyramidal molecules and the magnetic properties of E ground terms. *Inorg. Chem.* **8**, 491-497, (1969).
- 32 Morassi, R., Bertini, I. & Sacconi, L. Five-coordination in iron(II); cobalt(II) and nickel(II) complexes. *Coord. Chem. Rev.* **11**, 343-402, (1973).
- 33 Zhilinskaya, V. V., Kozlov, G. A., Nazarenko, Y. P. & Yatsimirskii, K. B. Electronic absorption spectra of cobalt (III) pentacyanide complexes. *Theor. Exp. Chem.* **16**, 402-406, (1981).
- 34 Gottesfeld, S. & McIntyre, J. D. E. Electrochromism in anodic iridium oxide films II. pH effects on corrosion stability and the mechanism of coloration and bleaching. *J. Electrochem. Soc.* **126**, 742-750, (1979).
- 35 Gorenstein, A., Da Fonseca, C. N. P. & Torresi, R. M. in *Optical Materials Technology for Energy Efficiency and Solar Energy Conversion X*. 104-116.
- 36 Burke, L. D., Lyons, M. E. & Murphy, O. J. Formation of hydrous oxide films on cobalt under potential cycling conditions. *Journal of Electroanalytical Chemistry and Interfacial Electrochemistry* **132**, 247-261, (1982).
- 37 Burke, L. D. & Murphy, O. J. Electrochromic behaviour of oxide films grown on cobalt and manganese in base. *Journal of Electroanalytical Chemistry and Interfacial Electrochemistry* **109**, 373-377, (1980).
- 38 Da Fonseca, C. N. P., De Paoli, M.-A. & Gorenstein, A. The electrochromic effect in cobalt oxide thin films. *Adv. Mater.* **3**, 553-555, (1991).
- 39 Patil, P. S., Kadam, L. D. & Lokhande, C. D. Studies on electrochromism of spray pyrolyzed cobalt oxide thin films. *Sol. Energy Mater. Sol. Cells* **53**, 229-234, (1998).
- 40 Yuan, Y. F. *et al.* Electrochromism in mesoporous nanowall cobalt oxide thin films prepared via lyotropic liquid crystal media with electrodeposition. *Journal of Membrane Science* **364**, 298-303, (2010).

- 41 Webster, R. D., Heath, G. A. & Bond, A. M. Voltammetric, EPR and UV-VIS-NIR spectroscopic studies associated with the characterisation of electrochemically generated tris (dithiocarbamate) cobalt (IV) complexes in dichloromethane. *J. Chem. Soc., Dalton Trans.*, 3189-3195, (2001).
- 42 Pinna, N. & Niederberger, M. Surfactant-free nonaqueous synthesis of metal oxide nanostructures. *Angew. Chem. Int. Ed.* **47**, 5292-5304, (2008).
- 43 Bilecka, I., Djerdj, I. & Niederberger, M. One-minute synthesis of crystalline binary and ternary metal oxide nanoparticles. *Chem. Commun.*, 886-888, (2008).
- 44 Toriumi, K., Ozima, M., Akaogi, M. & Saito, Y. Electron-density distribution in crystals of CoAl₂O₄. *Acta Crystallogr. B* **34**, 1093-1096, (1978).
- 45 Yang, J., Liu, H., Martens, W. N. & Frost, R. L. Synthesis and characterization of cobalt hydroxide, cobalt oxyhydroxide, and cobalt oxide nanodiscs. *J. Phys. Chem. C* **114**, 111-119, (2010).
- 46 Biesinger, M. C. *et al.* Resolving surface chemical states in XPS analysis of first row transition metals, oxides and hydroxides: Cr, Mn, Fe, Co and Ni. *Appl. Surf. Sci.* **257**, 2717-2730, (2011).
- 47 Brik, Y., Kacimi, M., Ziyad, M. & Bozon-Verduraz, F. Titania-Supported Cobalt and Cobalt-Phosphorus Catalysts: Characterization and Performances in Ethane Oxidative Dehydrogenation. *J. Catal.* **202**, 118-128, (2001).
- 48 Roth, W. L. The magnetic structure of Co₃O₄. *J. Phys. Chem. Solids* **25**, 1-10, (1964).
- 49 Maurizio, C. *et al.* XAS and GIXRD Study of Co Sites in CoAl₂O₄ Layers Grown by MOCVD. *Chem. Mater.* **22**, 1933-1942, (2010).
- 50 Brezesinski, T., Wang, J., Polleux, J., Dunn, B. & Tolbert, S. H. Templated Nanocrystal-Based Porous TiO₂ Films for Next-Generation Electrochemical Capacitors. *J. Am. Chem. Soc.* **131**, 1802-1809, (2009).
- 51 Wang, H.-Y. *et al.* In Situ Spectroscopic Identification of μ -OO Bridging on Spinel Co₃O₄ Water Oxidation Electrocatalyst. *J. Phys. Chem. Lett.* **7**, 4847-4853, (2016).
- 52 McCrory, C. C. L., Jung, S., Peters, J. C. & Jaramillo, T. F. Benchmarking heterogeneous electrocatalysts for the oxygen evolution reaction. *J. Am. Chem. Soc.* **135**, 16977-16987, (2013).
- 53 Zhang, J., Klasky, M. & Letellier, B. C. The aluminum chemistry and corrosion in alkaline solutions. *J. Nucl. Mater.* **384**, 175-189, (2009).
- 54 Lippens, P. E. & Lannoo, M. Calculation of the band gap for small CdS and ZnS crystallites. *Physical review. B, Condensed matter* **39**, 10935-10942, (1989).
- 55 Zhang, M., De Respinis, M. & Frei, H. Time-resolved observations of water oxidation intermediates on a cobalt oxide nanoparticle catalyst. *Nat. Chem.* **6**, 362, (2014).
- 56 Favaro, M. *et al.* Understanding the oxygen evolution reaction mechanism on CoO x using operando ambient-pressure X-ray photoelectron spectroscopy. *J. Am. Chem. Soc.* **139**, 8960-8970, (2017).
- 57 Huang, Z.-F. *et al.* Chemical and structural origin of lattice oxygen oxidation in Co-Zn oxyhydroxide oxygen evolution electrocatalysts. *Nature Energy* **4**, 329-338, (2019).
- 58 Ravel, B. & Newville, M. ATHENA, ARTEMIS, HEPHAESTUS: data analysis for X-ray absorption spectroscopy using IFEFFIT. *J. Synchrotron Radiat* **12**, 537-541, (2005).
- 59 Newville, M. IFEFFIT : interactive XAFS analysis and FEFF fitting. *J. Synchrotron Radiat* **8**, 322-324, (2001).
- 60 Lancashire, R. J. *Tanabe-Sugano diagrams via spreadsheets*, <<http://wwwchem.uwimona.edu.jm/courses/Tanabe-Sugano/TSSpread.html>> (2019).

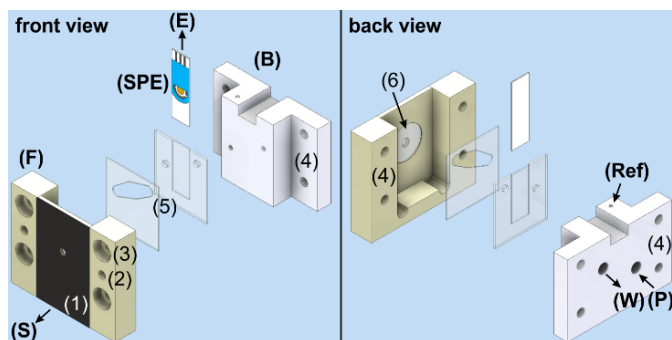


Figure 1. Design of the *operando* DRUV SEC. The PEEK front part (**F**) is covered with a black foil (1) and attached to the spectrophotometers (**S**) reflectance port by a mount and hold in place by magnets glued in cavities (2). The front is connected to the PTFE back (**B**) by nuts fixed in (3) and wing bolts going through holes (4). The electrode (**SPE**) is placed in the silicone gaskets (5) and connected to the potentiostat (**E**) by a connector cable. A Quartz window (6) is glued by silicone in a shallow cavity. The tip of the RHE reference electrode (**Ref**) is in contact to the electrolyte in the inlet channel. The electrolyte is flushed by a peristaltic pump (**P**) through PTFE tubes connected with HPLC fittings to the reservoir and the waste (**W**). A 3D-printed cover protects the setup from ambient light.

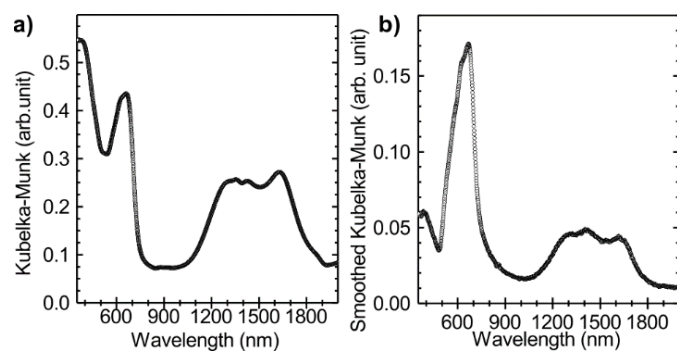


Figure 2. DRUV spectra of powdered $\text{Zn}_{0.35}\text{Co}_{0.65}\text{O}$ a) with BaSO_4 background and b) on Au working electrode of an SPE with the bare electrode as background.

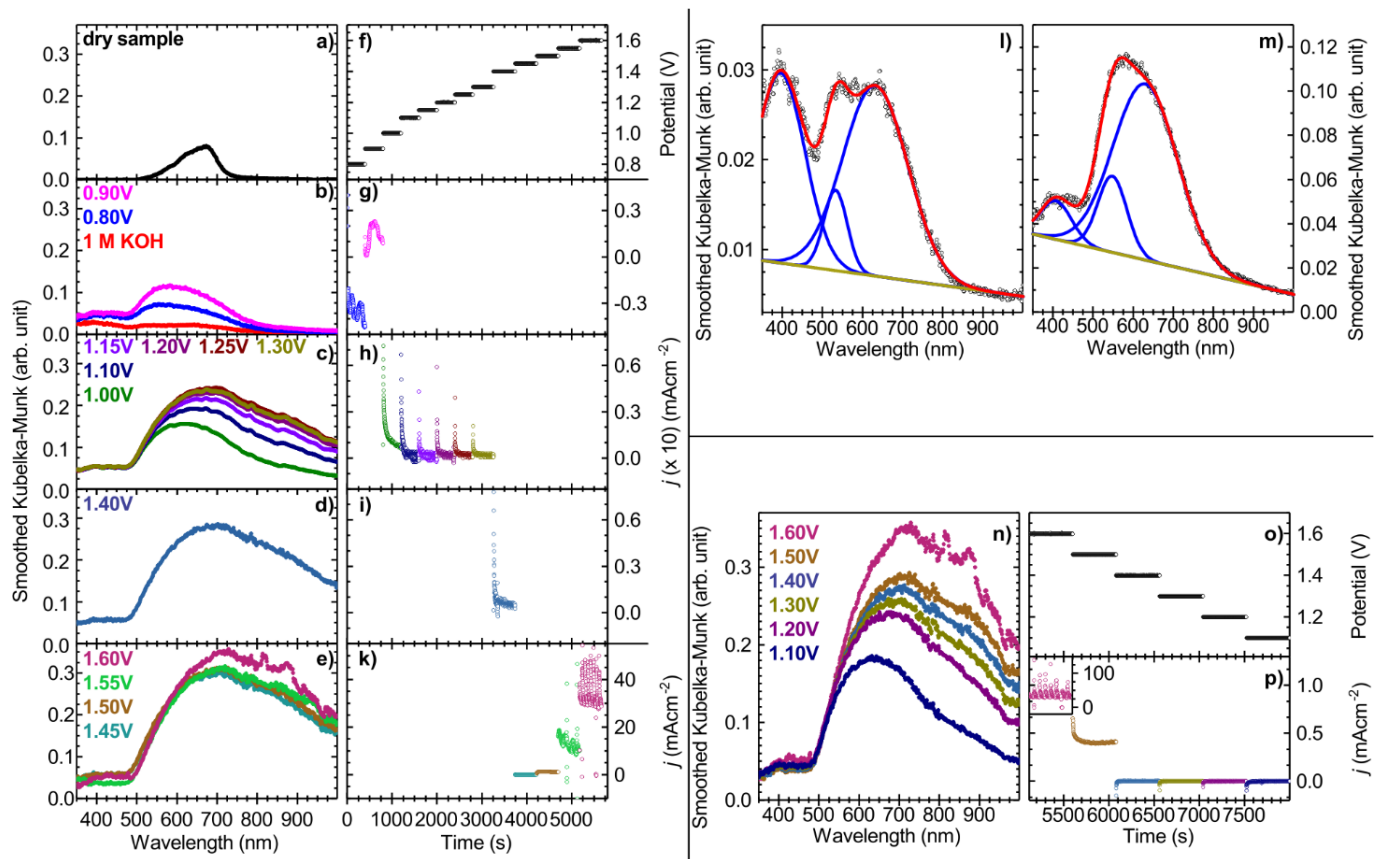


Figure 3. Operando DRUV spectroelectrochemistry of $\text{Zn}_{0.35}\text{Co}_{0.65}\text{O}$. a) DRUV spectrum of the dry sample on the SPE. b)-e) Spectra of the oxidation in 1 M KOH. f) Applied potential vs RHE as variation of time. g)-k) Corresponding current densities. The colors correspond to the applied potentials. l) Enlarged spectrum in 1 M KOH without applied potential. m) Enlarged spectrum at 0.9 V vs RHE. n) Spectra of the reduction in 1 M KOH. o) Applied potentials vs RHE as variation of time. p) Corresponding current densities. The inset in p) shows the current density at 1.6 V.

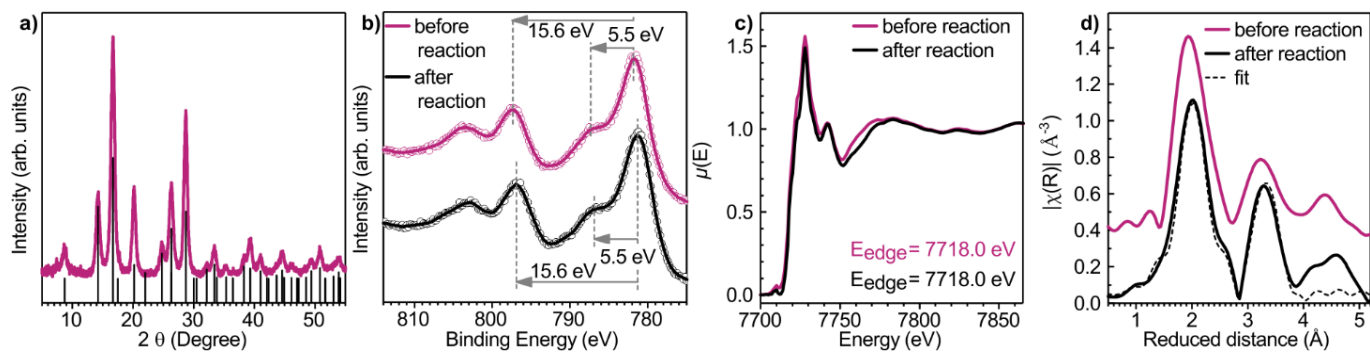


Figure 4. X-ray analyses on CoAl_2O_4 . a) XRD pattern of CoAl_2O_4 . Reference given is ICSD PDF-number 01-070-0753.⁴⁴ b) XPS spectra of CoAl_2O_4 before and after the reaction on the Co-edge. The peak positions and relative energy shifts point to an oxidation state of +II, before and after the reaction. c) XANES spectra of CoAl_2O_4 before and after reaction. d) Magnitude of the Fourier transforms of the recorded spectra of CoAl_2O_4 before and after reaction (k -range: 3.2–11.0). A fit was only possible for the latter.

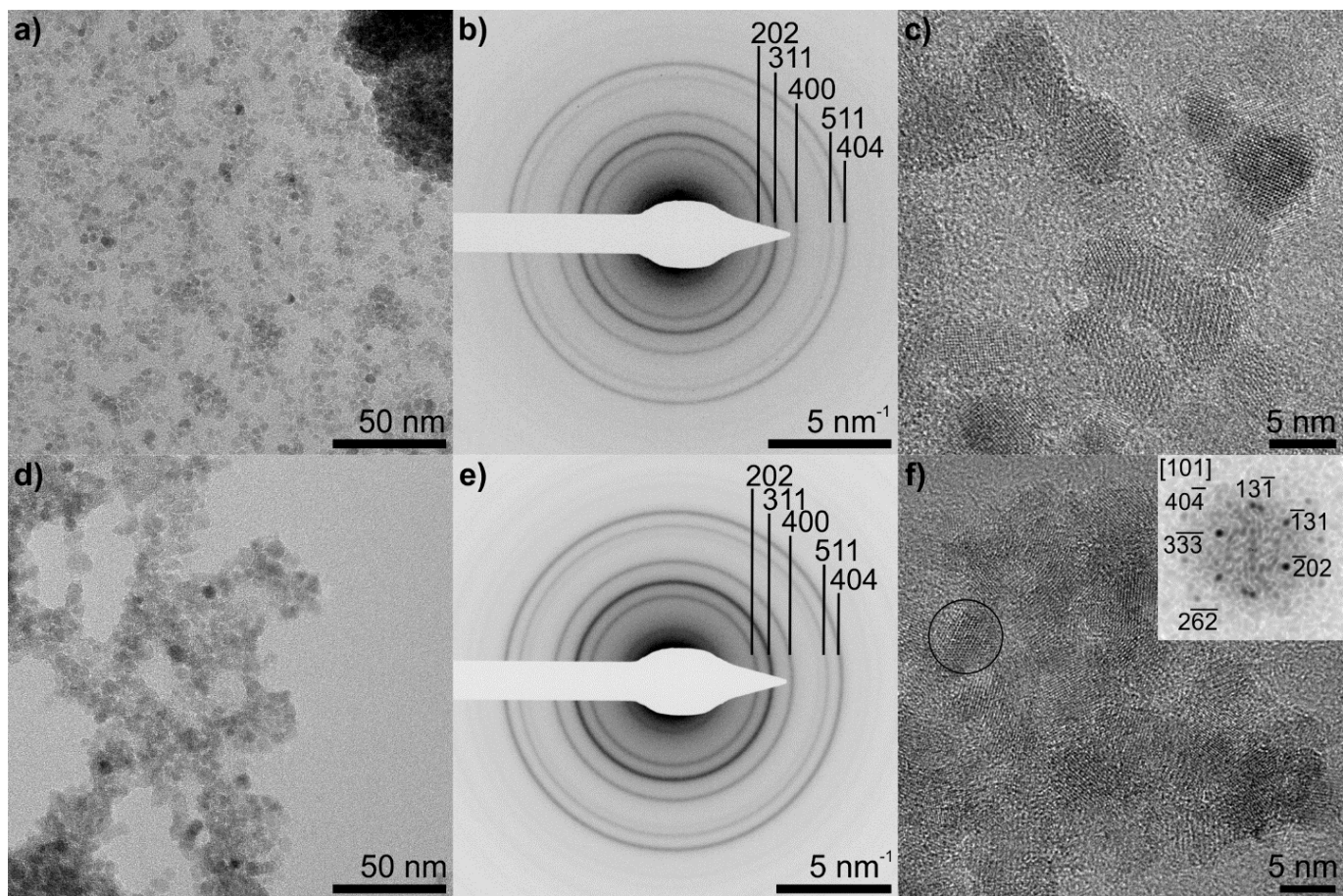


Figure 5. HRTEM micrographs of CoAl_2O_4 before (a-c) and after (d-f) 1 h electrochemical reaction at 10 mAcm^{-2} . a) and d) show an overview, b) and e) the SAED, with diffractions corresponding to spinel-type CoAl_2O_4 . c) and f) show high resolution micrographs. The inset in f) shows the power spectrum of the marked area. The spots are assigned to the $[101]$ zone axis of spinel-type CoAl_2O_4 .

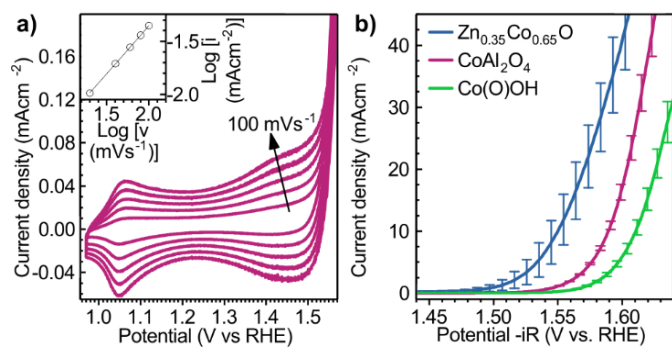


Figure 6. a) CVs of CoAl_2O_4 in 1 M KOH at different scan rates ν (20, 40, 60, 80 and 100 mVs^{-1}). From these, the oxidation peak current i for the redox-couple $\text{Co}^{2+/3+}$ was determined. The inset shows $\log(i)$ vs $\log(\nu)$. The slope of the linear fit is 0.9. b) LSV of $\text{Zn}_{0.35}\text{Co}_{0.65}\text{O}$, CoAl_2O_4 and Co(O)OH in 1 M KOH. The error bars indicate the deviation of three measurements.

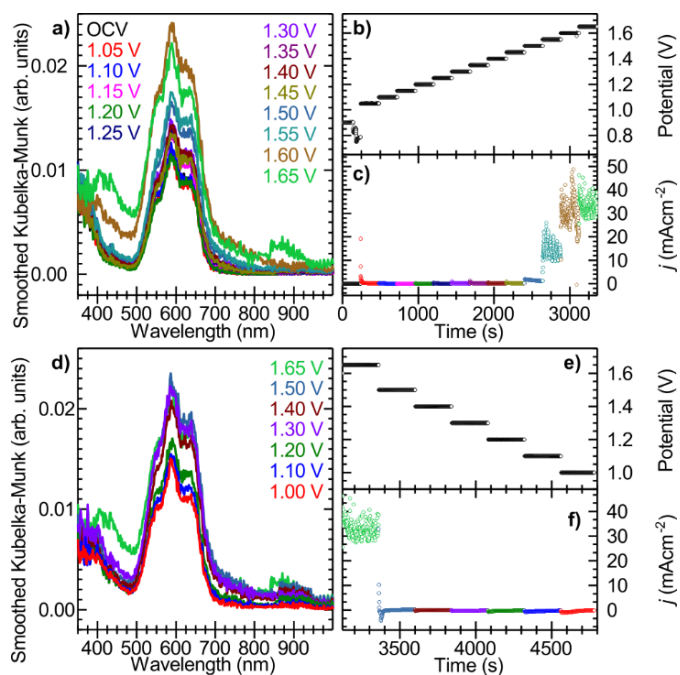


Figure 7: *Operando* DRUV spectroelectrochemistry of CoAl_2O_4 . a) and d) DRUV spectra in 1 M KOH for oxidation and reduction, respectively, b) and e) Applied potentials, c) and f) Corresponding CA measurements.

Table 1. EDX analysis of CoAl_2O_4 before and after electrochemical reaction.

	Co atom%	Al atom%
Before reaction	35.2	64.8
After reaction	40.0	60.0



TOC graphic